Applied Surface Science 542 (2021) 148723

Contents lists available at ScienceDirect

Applied Surface Science

journal homepage: www.elsevier.com/locate/apsusc

Full Length Article

Multifunctional environmental applications of ZnO nanostructures synthesized by the microwave-assisted hydrothermal technique

P.P. Ortega [a,*], C.C. Silva [a], M.A. Ramirez [a], G. Biasotto [b], C.R. Foschini [c], A.Z. Simões [a]

[a] São Paulo State University - UNESP, School of Engineering of Guaratinguetá, Av. Dr. Ariberto Pereira da Cunha 333, Guaratinguetá, SP, Brazil
[b] São Paulo State University - UNESP, Chemistry Institute, Professor Francisco Degni, Araraquara, SP, Brazil
[c] São Paulo State University - UNESP, Department of Mechanical Engineering, Av. Eng. Luiz Edmundo C. Coube 14-01, Bauru, SP, Brazil

ARTICLE INFO

Keywords:
Multifunctional materials
ZnO nanostructures
Photocatalysis
Gas sensors

ABSTRACT

Herein, we explore the multifunctional potential of ZnO nanostructures obtained via the microwave-assisted hydrothermal (MAH) method using a single synthesis route in the presence of CTAB. The ZnO samples were characterized by X-ray diffraction (XRD), Infrared Spectroscopy, Field Emission Gun Scanning Electron Microscopy (FEG-SEM), Transmission Electron Microscopy (TEM), photoluminescence properties (PL), as well as their photocatalytic activity and gas sensing response. XRD indicated that the ZnO nanostructures are free from impurities and crystallize in the hexagonal structure. FEG-SEM and TEM showed that rod-like ZnO nanostructures were obtained. Photoluminescence results indicate that the commercial ZnO sample has a higher bandgap and a more disordered crystalline structure compared with the ZnO nanostructures. The nanostructures presented superior photocatalytic performance, reaching 50% rhodamine 6-G photodegradation in 17 min, while the commercial sample took 43 min to reach the same value. The sensor film prepared from the ZnO nanostructures showed a fast response time of 10 s to 20 ppm of CO. The photocatalytic and gas sensing performances of the nanostructured ZnO highlights the multifunctional character of the nanostructures prepared via the MAH method and their potential for environmental applications such as water purification and air monitoring.

1. Introduction

Over the last decades, industrialization and urbanization growth have intensified water and air pollution, especially in densely populated areas. The implications of the constant emission of pollutants into the environment are alarming: cardiorespiratory and cardiovascular dysfunctions, stillbirth, impaired mental health, and disease proliferation are some of the consequences [1–3]. Therefore, the demand for environment-friendly policies and technologies able to remediate, reduce, or prevent pollution have increased significantly, being nanotechnology a distinct and up-and-coming field of research. Nanostructures have appealing advantages over conventional materials, such as small particle size, wettability, high surface energy, high reactivity, scalable fabrication, and high surface to volume ratio [4,5]. Particularly, the specific surface area of nanostructures is several orders of magnitude larger than in bulk materials, which increases their reactivity and make them attractive for catalytic applications. Large specific surface area is also crucial for gas sensing devices due to the availability of multiple adsorption sites for molecules of the target gas. In addition, the vast array of morphologies makes nanostructured materials a technological interest in many areas [6].

Among the numerous metal oxides explored throughout the years, the zinc oxide (ZnO) stands out due to being eco-friendly, low cost, nontoxic, possessing high electron mobility, wide bandgap (3.37 eV), and chemical stability, along with a variety of possible morphologies, size distributions and fabrication methods [7,8]. These properties highlight the multifunctional character of ZnO and its extensive list of applications, from bio and gas sensors to photocatalysis and optical devices [4,9,10]. As an attempt to enhance the performance of ZnO for specific purposes, several morphologies are being discussed in the literature. For instance, Zhu et al. [10] used the conventional hydrothermal method to synthesize different ZnO nanostructures by controlling parameters such as surfactant and mineralizer. They succeeded in obtaining nanoparticles, nanoplates, and nanoflowers and demonstrated that the gas sensing performance depends on the morphology. Suwanboon et al. [9] also proved the importance of nanostructures to the photocatalytic efficiency and antibacterial activity of ZnO. As can be seen, nanostructured zinc oxide is an attractive material regarding its ability to

* Corresponding author.
E-mail address: pedro.ortega@unesp.br (P.P. Ortega).

https://doi.org/10.1016/j.apsusc.2020.148723
Received 25 February 2020; Received in revised form 11 November 2020; Accepted 7 December 2020
Available online 10 December 2020

sense toxic and flammable gases (NO_2, CO, ethanol, H_2, ozone, etc.) [7,10–13] as well as purifying water from contaminants by photocatalytic processes [14], proving to be a valuable resource against air and water pollution. However, we are not aware of any scientific papers exploring the multifunctional potential of ZnO nanostructures obtained by the facile microwave-assisted hydrothermal method using a single synthesis route.

The synthesis method plays a critical role in the development of crystals and can diminish the ZnO potential due to the formation of undesired by-products, high defect density, or poor control of the nanostructure's characteristics [15]. Therefore, the microwave-assisted hydrothermal (MAH) method emerges as an advantageous synthesis route, capable of providing high-quality nanostructures, with good control over particle size distribution, chemical composition, phase formation, and morphology [16]. In the MAH synthesis, the nucleation of crystals starts once the ZnO concentration reaches supersaturation as a result of the dehydration of $Zn(OH)_4^{-2}$, which is the growth unit of ZnO nanoparticles [17–19]. In this way, the fast growth of ZnO nanocrystals leads to reduced specific surface areas and faces whose normal directions correspond to slow-growing dominate the final morphology [20–22]. Also, in the MAH method, the reaction takes place in a sealed autoclave, which prevents the release of chemicals into the air or water. Alongside other noticeable qualities such as low energy consumption, low cost, rapid volumetric heating, short reaction time, and high yield, the MAH method is a green approach to synthesize ceramic nanostructures [11,16]. CTAB is a cationic surfactant widely applied in the synthesis of nanomaterials, composed of a positively charged head and a long hydrophobic tail. It interacts electrostatically with $Zn(OH)_4^{-2}$, acting as a template for the growth of the nanostructures. Also, CTAB can form micelles in solution, playing a significative role in the properties and final morphology. Herein we report the use of CTAB combined with the microwave-assisted hydrothermal method to synthesize ZnO nanostructures and the analysis of their performance as a multifunctional material for carbon monoxide sensing and photocatalytic degradation of rhodamine 6-G. This research focuses not only on the synthesis and characterization but also on the relationship between structural defects and the sensor and photocatalytic properties of the nanostructures obtained at a low soaking time when compared with previous results [9,10].

2. Experimental procedure

2.1. Synthesis and characterization of the ZnO nanostructures

A quantity of 5×10^{-3} M of zinc acetate dihydrate ($Zn(CH_3COO)_2{\cdot}2H_2O$) was dissolved in a 2 M KOH (Merck P.A.) aqueous solution. After stirring for 15 min, 4.5 g of cetrimonium bromide (CTAB) was added to the solution and then transferred into a sealed Teflon autoclave and positioned in a hydrothermal microwave reactor (2.45 GHz, 800 W). The reactional system was then heat-treated at 120 °C for 8 min at a heating rate of 10 °C/min [11]. After the autoclave naturally cooled to room temperature, the resultant product was collected, washed multiple times with distilled water, and dried at 80 °C in an oven.

The obtained ZnO nanostructures were characterized by X-ray diffraction (XRD) using a Rigaku - DMax/2500PC diffractometer and Cu-Kα radiation (λ = 1.5406 Å) in the 2θ range from 20 to 80°. Scherrer's equation ($d = k\lambda/\beta\cos\theta$) was used to calculate the crystallite size (d) of the sample, where k is a constant, λ is the wavelength of the Cu-Kα radiation, β is the full-width at half maximum (FWHM) for the (1 0 1) reflection and θ is the diffraction angle of the main peak. The Fourier-transform infrared spectroscopy (FT-IR) spectrum was recorded to analyze the structural changes occurring during the MAH synthesis using the KBr pellet technique with a Bruker Equinox-55 equipment. The morphology of the ZnO nanostructures was observed using field emission gun scanning electron microscopy (FEG-SEM) with a Supra 35-VP (Carl Zeiss, Germany) microscope. Specimens for transmission electron microscopy (TEM) were obtained by drying droplets of as-prepared samples dispersed in an ethanolic solution, which had been sonicated for 5 min onto 300 mesh Cu grids. TEM, HRTEM images were then taken at an accelerating voltage of 200 kV on a Philips model CM 200 instrument. Photoluminescence spectroscopy (PL) was used to investigate the electronic transitions and the nature of defects within the samples. A 355 nm laser coupled to a mono-optical fiber was used as an excitation source, focusing the beam on the sample with a 1.6 mm spherical lens focus and 0.64 numerical aperture. Neutral density filters were used to control the laser power. The luminescence was collimated by the same lens and projected on a 50 μm multimode optical fiber. The emission spectra were deconvoluted using PeakFit v.4 software and fitted with Voigt area function.

2.2. Photocatalytic activity of the ZnO nanostructures

The photochemistry performance of the ZnO nanostructures was evaluated and compared to commercial ZnO purchased from Merck (99.98% purity). Tubes of 80 ml containing 1 mg of ZnO for every 1 ml were employed and immersed in an ultrasound bath (Glue 8850) for powder deagglomeration, leading to suspensions with high solid particle concentration. These suspensions presented 0.01 mM of rhodamine 6-G (Sigma P.A.). Therefore, all degradation process is carried out through the photocatalytic reaction of ZnO. To study the mechanism of action of the photocatalysts under the conditions described above, scavengers were added before the ultrasound bath: 1 mmol/disodium EDTA as an electronic hole scavenger (h^+), 1 mmol/L p-benzoquinone as a superoxide radical scavenger ($O_2^{\bullet-}$) and 200 mmol/L of isopropanol as a hydroxyl radical scavenger ($OH^{\bullet}$). P-Benzoquinone captures the photogenerated free electron and stabilizes it by resonance, preventing the formation of superoxides and hydroxyl radicals. The characteristic spectrum of the rhodamine 6-G (R6-G) displays an intense absorbance peak around 500 nm. The R6-G presence in the solution supplies an intense red-orange coloration. Its high absorptivity molar value (87.000 M^{-1} cm^{-1}) allows measuring the absorbance of specimens in solution even at low concentrations. Photocatalytic test measurements were performed from 0 to 16,000 s.

Absorbance data as a function of time were obtained from a light bulb that emits light in the ultraviolet region. Absorbance was monitored by means of 3 ml aliquots removed at different times. The data were acquired in a spectroscopy VARIAN model 5G. The suspensions were centrifuged (Fanem Ltda - Model 205N) to prevent light scattering during the experiment.

The specific speed constant (k) was obtained considering that electron-hole pairs are created by photons with energy superior to the bandgap energy, which promotes electrons to the valence band (VB) and leaves holes in the conduction band (CB), respectively. Therefore, the particular energies of these electrons and holes compared to an electrolyte allows the photoreaction to take place [23].

As with all heterogeneous catalysis reactions, the photoreactions in our research can be described as a first-class reaction. In this way, changes in the reactant concentration can be represented by a first-class equation of exponential decline, as represented by the Eq. (1).

$$A = A_0 e^{-kt} \tag{1}$$

where A is the concentration of the reacting species, A_0 is a daily pay-exponential constant, t is the reaction time, and k is the specific speed constant. The global reaction can be represented by:

$$R6 - G + \text{Surface} \xrightarrow{k} R6 - G^* + \text{Surface}^* \tag{2}$$

and the first-order speed reaction can be represented by the relationship:

$$v = k[A] \tag{3}$$

Considering that the concentration of reactant species decreases with time:

$$v = -\frac{d[A]}{dt} \quad (4)$$

and

$$A = \varepsilon bc. \quad (5)$$

where A the absorbance, b the optic way, c the concentration of the species, and ε the molar value of absorptivity.

Eq. (1) is obtained by integrating Eq. (5), in which A_0 is identified as the initial concentration of the reactant. Therefore, from this relation and using the absorbance value, it is possible to measure the specific speed constant for the reaction containing different oxides.

2.3. Fabrication, characterization and gas sensing response of the thick films prepared from the ZnO nanostructures

The nanostructured ZnO powder obtained by the MAH method was used to prepare thick films via the screen-printing technique, which is based on a paste prepared by mixing the nanostructured ZnO powder and an organic binder (glycerol) with a powder/binder ratio of 0.6 g/mL. The substrates on which the paste was deposited consisted of 96% dense insulating alumina with interdigitated electrodes delineated by sputtering. Once deposited, the thick films were heat-treated at 380 °C for 2 h in dry air atmosphere [24] to evaporate the binder. The electrical characterization was performed in a dry air, vacuum, and CO atmospheres in function of temperature and time in an optoelectronic device consisting of a closed chamber. Three cycles of heating in vacuum were done to assure the complete volatilization of humidity. The CO sensing tests were performed at 300 °C using a 20 V d.c. voltage. The sensor response was analyzed applying four different CO concentrations: 5, 10, 15, and 20 ppm. Conductance-time measurements were taken using a stabilized high voltage source measuring unit (Keithley, model 237) with a 1 s delay.

3. Results and discussion

3.1. Characterization of the ZnO nanostructures

3.1.1. X-ray diffraction (XRD) analysis

The ZnO nanostructures (Fig. 1a) were analyzed using XRD, which shows the formation of completely crystalline hexagonal ZnO (space group P63mc) in agreement with JCPDS card number 036-1451 [25]. No impurities or secondary phases were found. The narrowness of the peaks indicates good crystallinity, demonstrating the long-range periodicity of the zinc oxide obtained via the MAH method. The average particle size (d) of the nanostructures calculated based on Scherrer's equation is 3.9 nm. Evidence of the complete transformation of $Zn(OH)_x$ into ZnO is that the precursor, zinc acetate, is easily dissociable in water and the formed Zn^{4+} ions react spontaneously with KOH, producing a highly exothermic reaction. At the same time, potassium acetate (CH_3COOK) is formed as a by-product, which surrounds $Zn(OH)_x$ and avoids its overgrowth, leading to nanostructures with a rather small particle size distribution. Finally, the oxidizing atmosphere dehydrates the intermediate $Zn(OH)_x$ to ZnO.

3.1.2. FT-IR analysis

The presence of hydroxyl groups and other inorganic or organic contaminants in the ZnO sample was investigated by Fourier-transform infrared spectroscopy (FT-IR) in the mid-infrared range, from 400 to 4000 cm^{-1} (Fig. 1b). Characteristic *O–H* vibration modes attributed to absorbed water molecules on the sample's surface were found at 3400 ad 1600 cm^{-1} [26]. The bands at 2300 and 1000 cm^{-1} corresponds to the *C=O* vibration mode of CO_2 present in the air. The FT-IR modes at

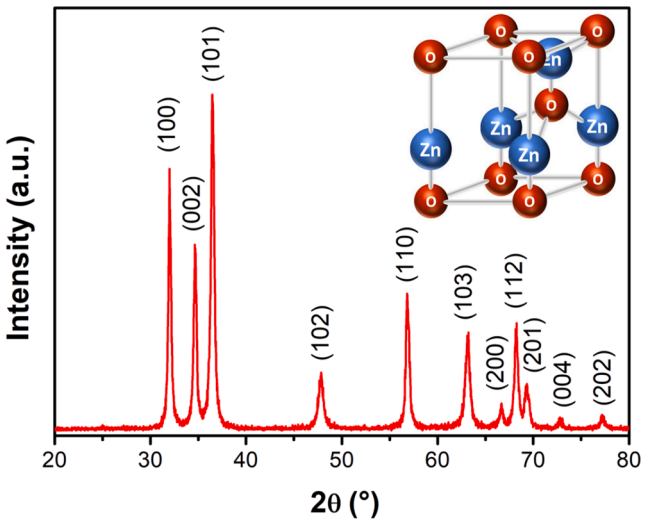

(a)

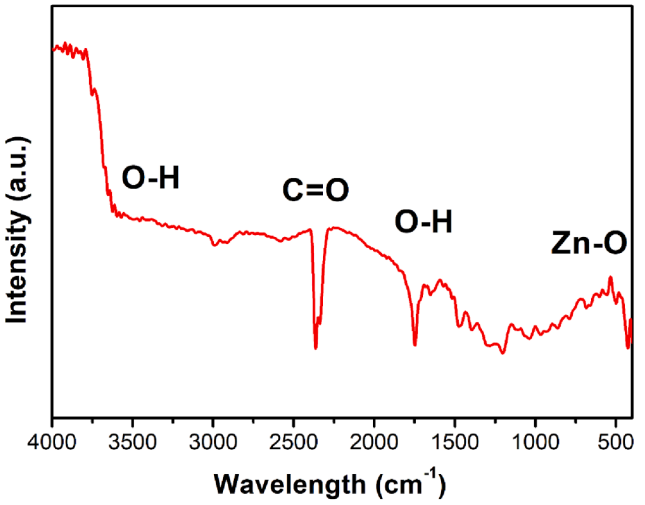

(b)

Fig. 1. XRD (a) and FT-IR (b) pattern of the ZnO nanorods obtained in the hydrothermal microwave method at 120 °C for 8 min.

900, 1000, 1350, and 1500 cm^{-1} are similar to those of ZnO nanoparticles [26]. The intense wide band below 700 cm^{-1} belongs to the *Zn–O–Zn* vibration modes. The strong absorption bands at 400–600 cm^{-1} are due to the bending (δ) and stretching (ν) of Zn–O, which are characteristic of the tetrahedral groups (ZnO_4) in the sample. No traces of contaminants or impurities from raw precursor and the surfactant (C, H, Br, and N bonds) were found, indicating that the MAH method allows obtaining nanostructures at low temperatures and short soaking time.

3.1.3. Morphological analysis of the ZnO nanostructures

As shown in the transmission electron microscopy (TEM) in Fig. 2a, typical nanorod morphology was formed for the ZnO sample. The inset on the bottom left corner illustrates the field emission gun scanning electron microscopy (FEG-SEM). The nanorods exhibit hexagonal cross-section and weak aggregation, which is an indication that Van der Waals forces are reduced. Also, the sample presented homogenous size distribution, with 50–400 nm in width and about 1 μm in length. The nanorods grew preferably in the (101) and (100) orientations, suggesting there is a certain preference for the growth of the nanostructures in the *h*00 axis. This is associated with the displacement of the ZnO mode to lower energy, giving freedom to the structure and to greater relations of oxygen vacancies. Fig. 2b depicts the atomic resolution image of the

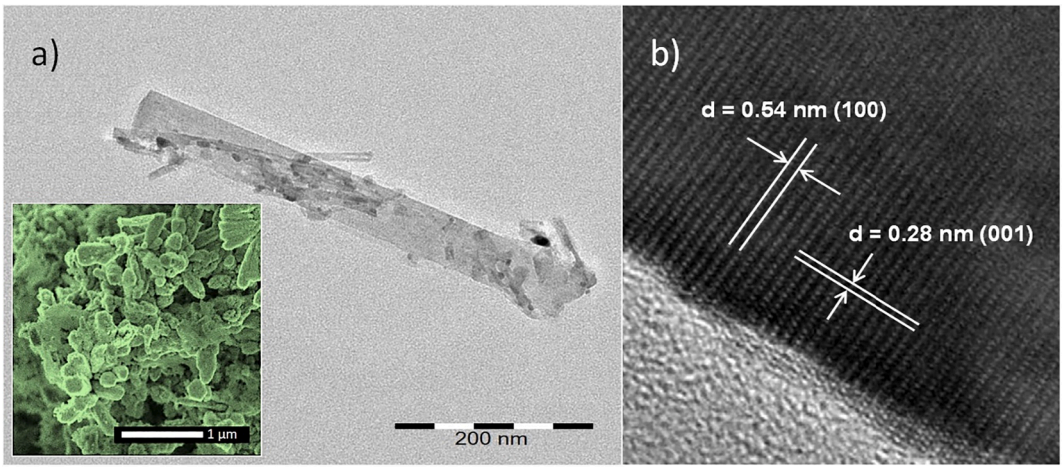

Fig. 2. TEM micrography of the ZnO nanorods obtained via MAH method at 120 °C for 8 min. Inset illustrates the FEG-SEM image of the nanorods.

sample, in which the interplanar distances (d) for the (1 0 0) and (0 0 1) planes are 0.282 and 0.541 nm, respectively. These values are compatible with the JCPDS card 036-1451 and assure the high crystallinity of the ZnO phase, as described previously in the XRD analysis. In other words, the MAH method allows the formation of a long-range ordering of the ZnO hexagonal crystalline structure. During the MAH synthesis, a large amount of nucleation sites is present in the solution, and considering that it is highly diluted, as the reaction continues, there are not enough reactants left to contribute to the growth of the particles. Therefore, the mean particle size distribution of the nanostructures is limited, preventing their overgrowth. Moreover, the MAH method provides rapid heating and increased mobility for the ions and molecules in the solution, which accelerates them to high velocities, promoting higher collision rate and better effective fusion at the collision point [17,27]. Furthermore, the rapid growth of the particles leads to the formation of Zn and O vacancies, which might contribute to different size distributions.

Fig. 3 illustrates the possible growth mechanism of the ZnO nanorods during the MAH synthesis. In the hydrothermal solution, $Zn(OH)_4^{2-}$ anions are formed after the addition of KOH to a zinc acetate dihydrate solution. CTAB is a cationic surfactant that dissolves completely in water, resulting in CTA^+ cations consisting of long hydrophobic tails and positively charged hydrophilic heads. Then, when added to the hydrothermal solution, these cations will interact electrostatically with Zn $(OH)_4^{2-}$ and form ion-pairs. Due to its hydrophobic/hydrophilic characteristics, the surfactant tends to aggregate in water in the form of micelles. The micelle's shape determines the final morphology of the nanostructure. Therefore, the formation of rod-like shaped micelles will lead to rod-like nanostructures. The presence of CTAB also reduces the surface tension of the solution, allowing the crystallization of the ZnO phase with lower energy requirements, that is, at lower temperatures and short reaction time [28,29]. Moreover, the microwave radiation acts directly on the permanent dipole of water and enhances the crystallization kinetic behavior by one or two orders of magnitude [30].

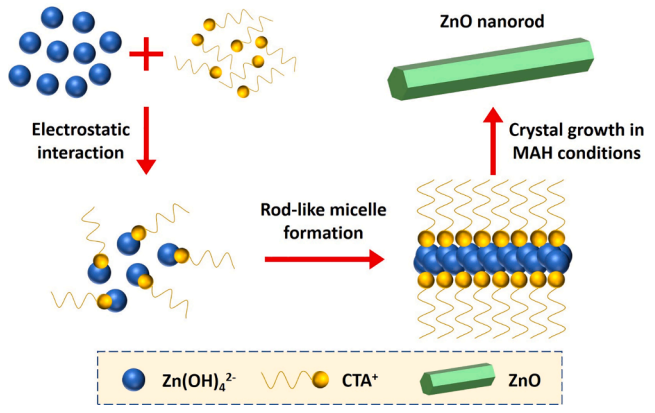

Fig. 3. Schematic diagram showing the growth of the ZnO nanostructures in the presence of CTAB during the MAH synthesis.

3.1.4. *Photoluminescence analysis of the ZnO nanostructures*

Photoluminescent emissions result from the electromagnetic radiation released by electronic transitions between an excited energy state and the fundamental state of an electron [31]. These emissions depend on structural distortions and defects, which create localized energy levels inside the bandgap and increase the radiative contribution with the energy difference between these levels [32]. Therefore, the structural order-disorder degree is inversely proportional to the recombination rate of excitons, increasing the emission intensity [33]. In photocatalysis, the electron-hole recombination rate is a crucial parameter since low recombination rates increase the number of charge carriers available to initiate oxireduction reactions of dissolved species and organic compounds. Mono ($V_O^{\cdot}$) and doubly ionized ($V_O^{\cdot\cdot}$) oxygen vacancies are structural defects mostly related to the wide-range emission in the visible spectrum. These two vacancies capture and trap excited electrons during their decay, resulting in the emission of specific photons with wavelengths equivalent to the energy difference between the electronic levels.

In the photoluminescence spectra of the nanostructured ZnO (Fig. 4), the blue (472 nm) and green (555 nm) bands correspond to 20 and 42% of the emissions, respectively. Both bands are related to the presence of mono-ionized oxygen vacancies. These defects, known as shallow defects, are localized close to the conduction or the valence band and represent high energy emissions (blue and green) [34]. On the other hand, small energy emissions (red) correspond to the direct radiative decay of excitons [35]. An increase in the emission percentage of the red region compared to the blue region indicates a lower proportion of defects inside the bandgap able to inhibit the direct recombination, which results in a higher emission percentage of these states in the total emission of the sample. Also, we can see a low-intensity emission at 796 nm. Doubly ionized oxygen vacancies are energetically close to the Fermi level and correspond to low energy emissions in the yellow-red regions [36], being classified as deep defects. In the photoluminescent spectrum of the commercial ZnO – besides emissions in the blue (469 nm), green (555 nm), and red (694 nm) regions –, two additional intense bands appear at 627 nm and 776 nm, with 28 and 17% of the total emission, respectively. This broader spectrum of the commercial sample with a higher contribution of oxygen vacancies to the emission spectrum can be associated with a higher bandgap value.

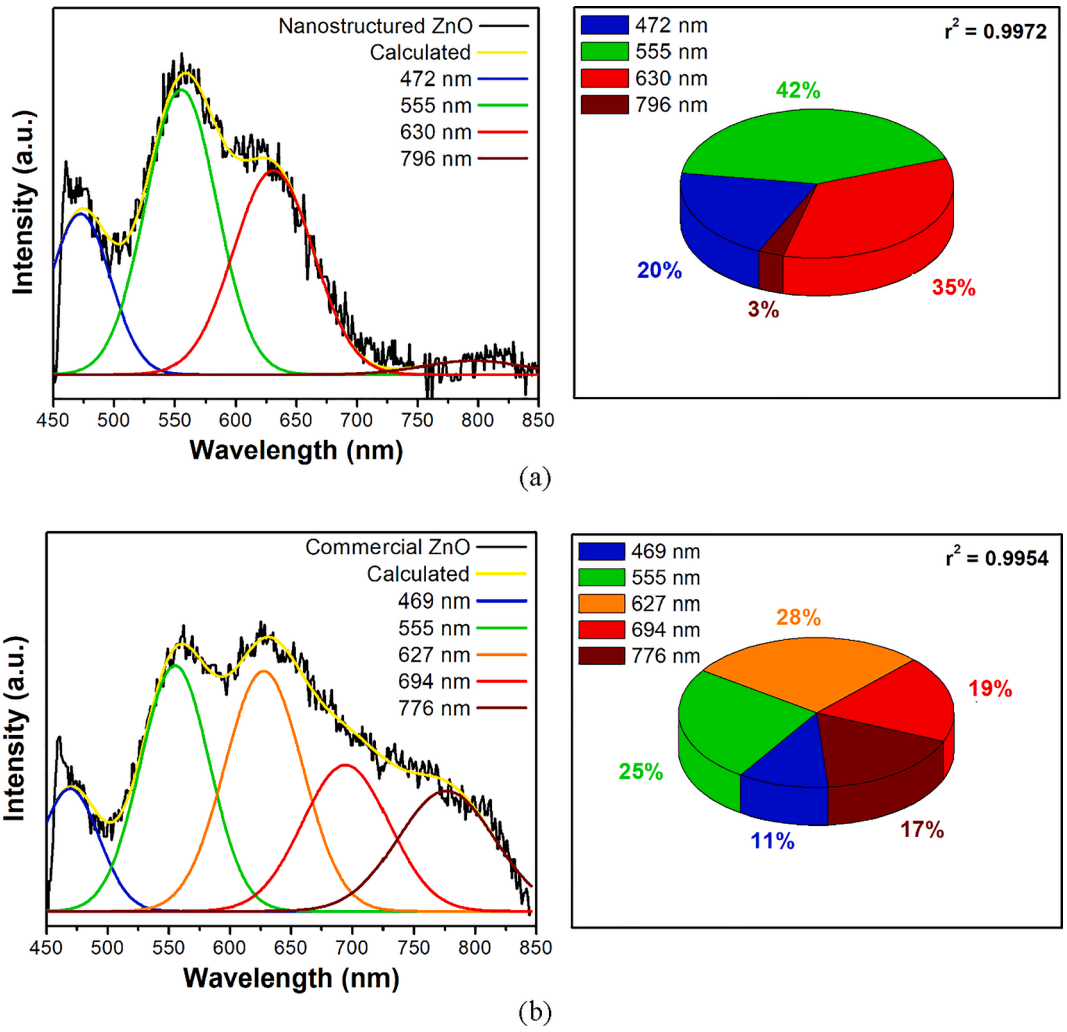

Fig. 4. Deconvolution of the photoluminescence spectra and emission percentage of the ZnO nanostructures (a) and the commercial ZnO (b).

From such results, we conclude that the bands observed in the photoluminescent spectrum are associated with the direct recombination of electrons in the Zn 4p conduction band with holes in the O 2p valence band. The broad emission band suggests the presence of many point defects, such as oxygen vacancies. The higher intensity emission spectrum of the commercial ZnO indicate that it has a more disordered crystalline structure than the nanostructured ZnO. We discarded transitions involving interstitial oxygen ions due to the absence of a photoluminescent band associated with the yellow emission around 2.18 eV.

3.2. Photocatalytic activity of the ZnO nanostructures

The decay spectra corresponding to the rhodamine 6-G (R6-G) degradation in the presence of nanostructured and commercial ZnO are shown in Fig. 5. Due to the photocatalytic action of ZnO, the decomposition of the R6-G molecule was clearly observed. The nanostructures (Fig. 5a) presented higher photocatalytic activity when compared to the commercial sample (Fig. 5b), which may be due to the accumulation of electrons and recombination time of electron-hole pairs in the nanostructures. There are two main routes responsible for the photodegradation of dyes such as rhodamine 6-G: (1) direct oxidation by charge transfer between dye and formed holes ($h^{\bullet}$) or photoelectrons (e') in the semiconductor or (2) by the creation of reactive oxygen species such as OH radicals (OH*) and superoxides (O_2H^*). Electron-hole pairs are created by irradiating the semiconductor with an electromagnetic radiation source with energy superior or equal to its band gap energy, which excites electrons to the conduction band and leaves electronic holes in the valence band. Then, electrons can react with oxygen species to form superoxide radicals ($O_2^{\bullet-}$), just as electronic holes (h^+) can react with water or adsorbed hydroxyl ions generating hydroxyl radicals ($OH^{\bullet}$). These three chemical species have a photocatalytic effect on R6-G discoloration, according to Eqs. (6)–(13):

$$\text{Photocatalyst} + h\upsilon \rightarrow \text{Photocatalyst}\ (e^-_{CB} + h^+_{VB}) \quad (6)$$

$$\text{Photocatalyst}\ (e^-_{CB}) + O_2 \rightarrow \text{Photocatalyst} + O_2^{\bullet-} \quad (7)$$

$$\text{Photocatalyst}\ (h^+_{VB}) + H_2O_{ads} \rightarrow \text{Photocatalyst} + H^+ + OH^{\bullet}_{ads} \quad (8)$$

$$\text{Photocatalyst}\ (h^+_{VB}) + OH^-_{ads} \rightarrow \text{Photocatalyst} + OH^{\bullet}_{ads} \quad (9)$$

$$\text{Photocatalyst}\ (h^+_{VB}) + \text{R6-G} \rightarrow \text{R6-G}^{\bullet} + \text{R6-G oxidation} \quad (10)$$

$$OH^{\bullet}_{ads} + \text{R6-G} \rightarrow \text{R6-G discoloration} \quad (11)$$

$$O_2^{\bullet-} + \text{R6-G} \rightarrow \text{R6-G discoloration} \quad (12)$$

$$e^-_{CB} + h^+_{VB} \rightarrow \text{heat} \quad (13)$$

Scavenger tests were performed to compare the photocatalytic action of the species. Table 1 shows the photocatalytic activity of commercial and nanostructured ZnO when EDTA-Na_2, isopropanol, and p-benzoquinone were used as electronic hole (h^+), hydroxyl ($OH^{\bullet}$), and superoxide ($O_2^{\bullet-}$) radical scavengers, respectively. The percentages were calculated based on 120 min of reaction time. The use of EDTA-Na_2 and

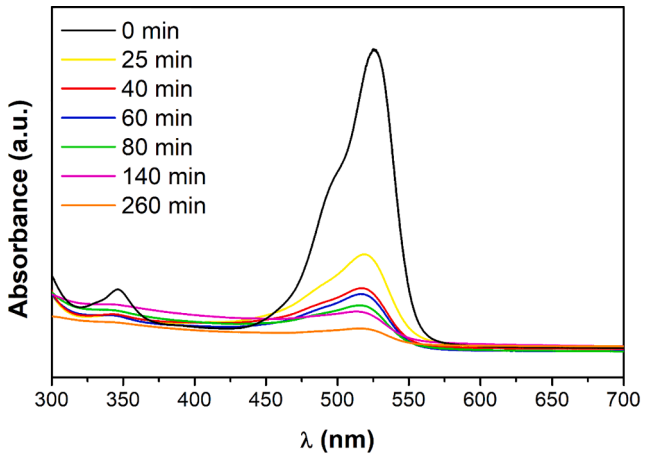

(a)

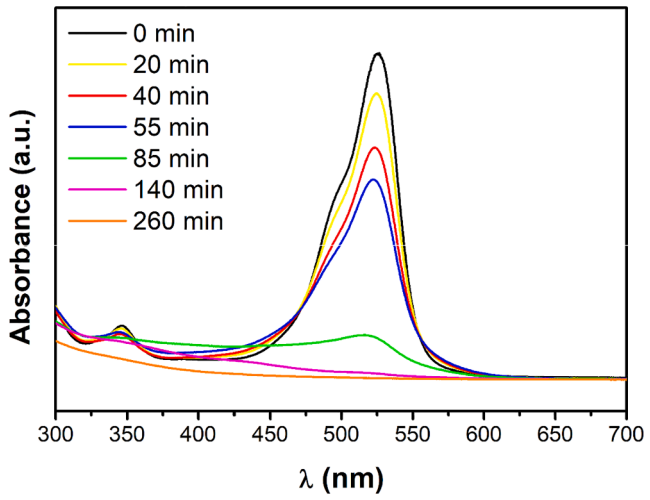

(b)

Fig. 5. Concentration decay spectra of the R6-G molecule as a function of different time intervals in the ultraviolet light region for the ZnO nanostructures (a) and commercial ZnO (b).

Table 1
R6-G discoloration after 120 min under UV light using ZnO nanostructures and commercial ZnO with and without scavengers.

System	ZnO nanostructures (% disc.)	ZnO (Merck) (% disc.)
Without scavenger	86.0	82.2
(- h^+)	51.2	42.7
(- $OH^•$)	48.4	39.9
(- $O_2^{•-}$)	27.3	24.4

isopropanol led to a dye discoloration reduction of approximately 40%, demonstrating that both h^+ and $OH^•$ species have similar activity. Among the photogenerated species, the superoxide radical ($O_2^{•-}$) presented the most relevant reduction in discoloration (~27%). Our results are in agreement with the study performed by Liu [37], which has also shown the superoxide radicals as the most photoactive species, unlike the findings previously reported by other authors [38–41].

The photocatalytic mechanism of ZnO is based on the adsorption of water molecules in its surface, promoting different types of radicals and leading to high photocatalytic activity, which is attributed to the indirect sensitization of the rhodamine 6-G. In this case, electrons are transferred from the dye to the conduction band and then interact with the adsorbed species on the catalyst surface, producing radical species that act on dye degradation [42]. The electrons injected into the conduction band of the photocatalyst play a significant role in the formation of superoxide radicals, which in turn can create hydroxyl radicals, according to Eqs. (14)–(20):

$$\text{R6-G} + h\nu \rightarrow \text{R6-G}^{+} + e^{-} \quad (14)$$

$$e^{-} + \text{Photocatalyst} \rightarrow \text{Photocatalyst}\,(e^{-}_{CB}) \quad (15)$$

$$\text{Photocatalyst}\,(2e^{-}_{CB}) + O_2 + 2H^{+} \rightarrow H_2O_2 + \text{Photocatalyst} \quad (16)$$

$$2O_2^{•-} + 2H^{+} \rightarrow H_2O_2 + O_2 \quad (17)$$

$$H_2O_2 + \text{Photocatalyst}\,(e^{-}_{CB}) \rightarrow OH^{\bullet} + OH^{-} + \text{Photocatalyst} \quad (18)$$

$$H_2O_2 + O_2^{•-} \rightarrow OH^{•} + OH^{-} + O_2 \quad (19)$$

$$H_2O_2 + h\nu \rightarrow 2OH^{•} \quad (20)$$

The photocatalysis data indicate that the growth of zinc oxide crystals in the presence of surfactant generated defects which acted as trappers of the charge carriers, increasing the recombination time of the photogenerated exciton. As CTAB has a higher boiling point than water, it is reasonable to assume that CTAB will attach to the nanostructures, leading to a product with hydrophilic characteristics and many nucleation sites with uniform size and controlled morphology. Consequently, the surfactant-assisted synthesis changes the structural defects or creates additional states localized inside the bandgap.

Therefore, photocatalysts whose excitons are separated by a longer energetic gap tend to be more photoactive since recombination is thermodynamically more difficult, increasing recombination time. That indicates the possible paths of exciton recombination for the nanostructured ZnO while those related to the commercial sample limit the paths of recombination of the e^{-}/h^{+} pair. Photogenerated carriers are created upon the incidence of radiation on a photocatalyst species, causing the oxidation of dyes and other organic pollutants following their adsorption on the photocatalyst surface. The oxidation process can be direct or indirect. The direct oxidation promotes degradation through electron transfer between the organic compound and the semiconductor's surface. The indirect oxidation – the most common degradation mechanism – is controlled by photogenerated carriers such as OH* radicals, which are formed by the oxidation of water or hydroxyl ions adsorbed on the photocatalyst surface.

The absorbance decay of the R6-G molecule as a function of time in the ultraviolet light region for the nanostructured and commercial ZnO

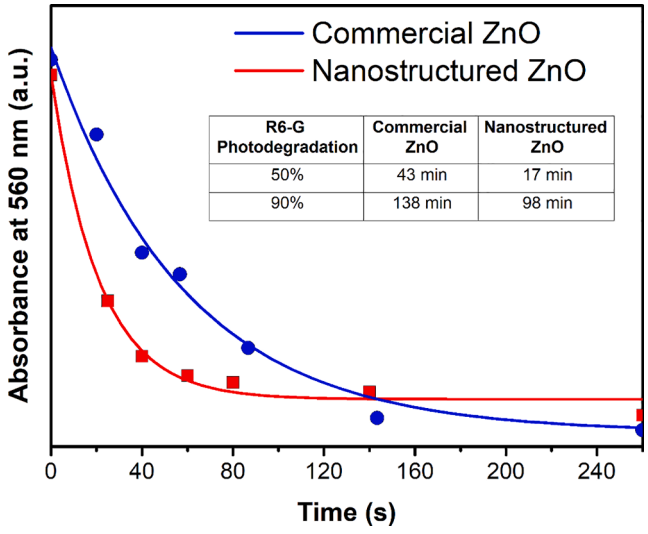

Fig. 6. Absorbance decay for the R6-G molecule as a function of time in the ultraviolet light region at 560 nm for the ZnO nanostructures and commercial ZnO.

is illustrated in Fig. 6. The absorbance decay is sharper for the nanostructured sample, indicating its fast photodegradation of the R6-G molecule. Indeed, commercial ZnO took 43 min to reach 50% R6-G degradation, while nanostructured ZnO took only 17 min. This confirms our previous observation that the nanostructures obtained by the MAH method have higher activity than the commercial ones due to the electrons injected into the photocatalyst, which leads to superoxide radicals as OH* and O_2H* as well as charge transfer between the organic compound and formed holes (h˙) or photoelectrons (e′) in the material.

The normalized speed constant (k) values to the surface area are presented in Table 2. The availability of adsorption sites on a semiconductor's surface increases proportionally with the specific surface area (SSA), consequently improving the photocatalytic performance and reaction speed. It becomes clear by analyzing Table 2 that the ZnO nanostructures performed better than the commercial sample due to superior k values and higher SSA, a behavior noticed even without normalization.

The better photocatalytic performance of the ZnO nanostructures obtained by the MAH method can be associated with its SSA as well as the reduction of the bandgap energy. Defects and morphology are other factors that certainly contribute to the photocatalytic activity. Factors such as surface energy and adsorption of the reacting species must be decisive for the observed improved performance. One advantage to employ ZnO nanostructures in photocatalytic reactions is the method of synthesis. By carefully controlling the pressure, time, surfactant, and crystallization temperature it is possible to tune the properties of the samples in the hydrothermal microwave reactor and design nanomaterials with better photocatalytic performance.

The optical band gap energy (E_{gap}) was calculated by the method proposed by Kubelka and Munk [43], as previously described by the group [11]. Fig. 7 illustrates the UV–Vis spectra and the estimated direct E_{gap} of nanostructured and commercial ZnO with an uncertainty of 0.05 eV. The E_{gap} of the nanostructured sample is lower than those synthesized by different methods [44]. In addition, the energy gap for the commercial ZnO is slightly higher. The intrinsic bandgap can be represented as an intermediate energy level between the VB and the CB of ZnO. These results confirm that the modification of the E_{gap} is associated with the visible active nanostructures through UV–vis spectra shoulders in the visible region. However, the main changes in the optical energy gap can be associated with structural defects or additional states localized inside the bandgap. These defects might result from two factors: changes in the surface area and distinct types of oxygen vacancies. An increase in the number of defects leads to the formation of localized states within the bandgap due to the corresponding increase of vacancies. This behavior is an indication that these samples present a certain structural disorder degree.

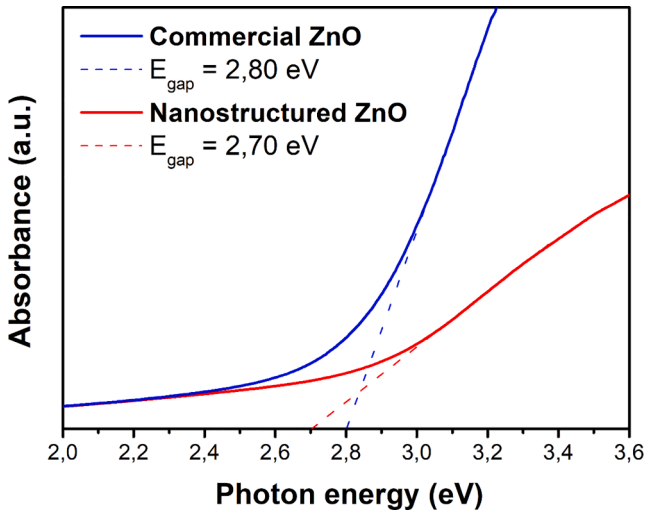

Fig. 7. Diffuse reflectance spectra of the ZnO nanostructures and the commercial ZnO.

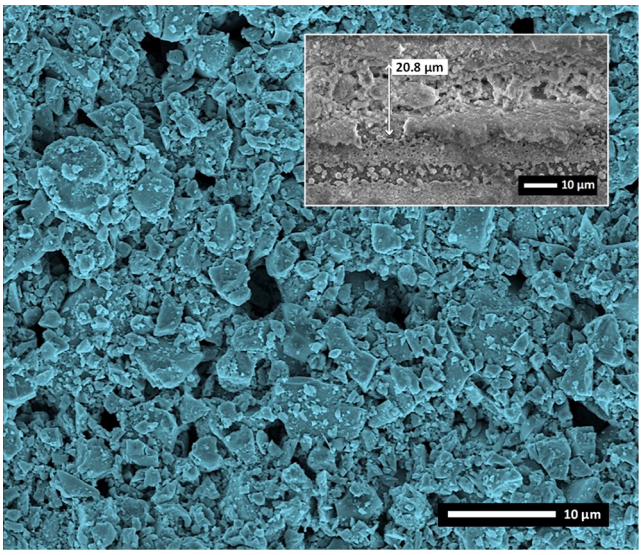

Fig. 8. Schematic diagram showing the resistance variation of the nanostructured ZnO film during interaction with gas molecules.

3.3. Characterization and sensor response of the thick films prepared from ZnO nanostructures

3.3.1. FEG-SEM analyses

The FEG-SEM micrography of the thick film (Fig. 8) shows that the nanostructures tend to form large agglomerates, possibly due to Van der Waals forces arising from hydroxyl groups introduced by the organic binder (glycerol) during the film preparation. The transversal section of the film (inset in Fig. 8) shows that its thickness is about 20 µm. To minimize surface energy, the primary nanostructures in the hydrothermal solution tend to form approximately spherical agglomerates with reduced surface/volume ratio, therefore minimizing the surface free energy. The reactions taking place during the MAH synthesis can be described by "dissolution and crystallization" processes. The $Zn(OH)_x$ formed during the mixing of the precursors dissolves by the action of KOH and reacts at high pressures and temperatures, resulting in the precipitation of insoluble ceramic nanostructures.

Table 2
Normalized k values by the specific surface area of the samples and its average quadratic error.

Systems	k (s^{-1}) × 10^{-4}	k (g/m^2s) × 10^{-6}	$e^{2\text{Å}}_{x}$ 10^{-3}	Specific surface area (m^2/g)
Commercial ZnO	2.84	2.47	14.6	9.2
Nanostructured ZnO	8.96	7.17	6.74	10.8

3.3.2. Sensor properties

For an n-type semiconductor, three different types of oxygen species will form on the surface depending on the temperature: O_2^- (below 100 °C), O^- (between 100 and 300 °C), or O^{2-} (above 300 °C). These species react with CO to form CO_2, which increases the conductivity of the sample. Therefore, higher temperatures lead to high sensitivities to the target gas since more electrons are involved in the reaction. As illustrated in Fig. 9, when the oxygen molecules adsorb (step 1) onto the surface of the ZnO nanorods, they trap electrons from the conduction band (step 2) to form oxygen species (step 3), thus reducing the number of charge carriers (e-) available and decreasing the conductivity.

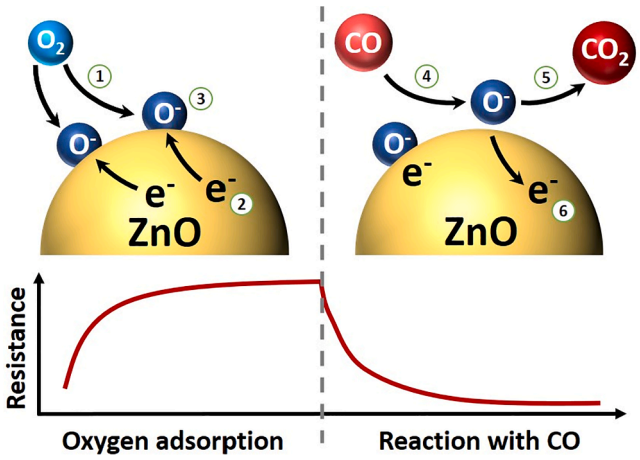

Fig. 9. FEG-SEM and inset of the transversal section of the films prepared from the ZnO nanorods obtained via the MAH method at 120 °C for 8 min.

Contrarily, the reaction with CO (step 4) extracts adsorbed and diffused oxygen species (step 5) from the sample, releasing the previously trapped electrons back to the conduction band (step 6), thus increasing the conductivity. The conductivity variation of ZnO when exposed to CO provides a measurable response, allowing the detection of this highly toxic gas.

It is common knowledge that an oxygen vacancy acts as an electron donor, and its presence tends to increase the conductivity of the sample. Consequently, when all the adsorbed oxygen is consumed in the reaction with CO, diffused oxygen moves out of the grains to keep the reaction going. This process increases the number of oxygen vacancies, which in turn increases the conductivity. This behavior is strongly associated with the effect of the oxygen adsorption onto the surface on the potential barrier height (PBH) of the sample. The PBH acts as an obstacle to electron mobility inside the semiconductor, and oxygen adsorption tends to increase the PBH, resulting in low conductivity. Besides, oxygen diffusion into the grains (a process that also reduces the conductivity of the sample) is not relevant at temperatures below 270 °C, and the conversion rate of CO to CO_2 intensifies from 200 to 350 °C. Therefore, we can assume that this reaction is favored as temperature and CO concentration increase, resulting in a more conductive sample.

The sensitivity (S) to a particular gas is defined by $S = R_{gas}/R_{vac}$, where R_{gas} is the film's electrical resistance when exposed to the target gas (air, O_2, or CO) after reaching equilibrium, and R_{vac} is the film's electrical resistance in vacuum conditions. To determine the working temperature (the temperature in which the sensitivity to CO is the highest) of the nanostructured ZnO films, we monitored their sensitivity to air and CO as a function of temperature, as shown in Fig. 10a. The sensitivity to CO (R_{CO}/R_{vac}) reaches its peak around 350 °C, which we determined as the working temperature for the nanostructured ZnO films. It is worth mentioning that the lower the working temperature, the more advantageous it will be due to a reduction in operating costs and energy consumption. The R_{CO}/R_{vac} ratio is close to 0.25 at 350 °C, mainly due to a sharp decrease in the film's electrical resistance when exposed to CO (R_{CO}), as expected for an n-type semiconductor in a reducing atmosphere. The large sensitivity difference between air and CO – R_{air}/R_{vac} is much higher than R_{CO}/R_{vac} – indicates that the nanostructured ZnO films can detect the presence of CO in the air atmosphere.

To study the film response to CO, we monitored their electrical resistance in function of time under air and CO atmospheres (Fig. 10b). The resistivity of the film decreases rapidly upon reaction with CO (gas in), and it only recovers its original value once clean air replaces CO in the gas chamber (gas off). The response of our film to CO is rapid, with a response time (t_{resp}) of 10 s in 20 ppm and 26 s in 5 ppm. The saturation time is usually different for adsorption and desorption processes. After

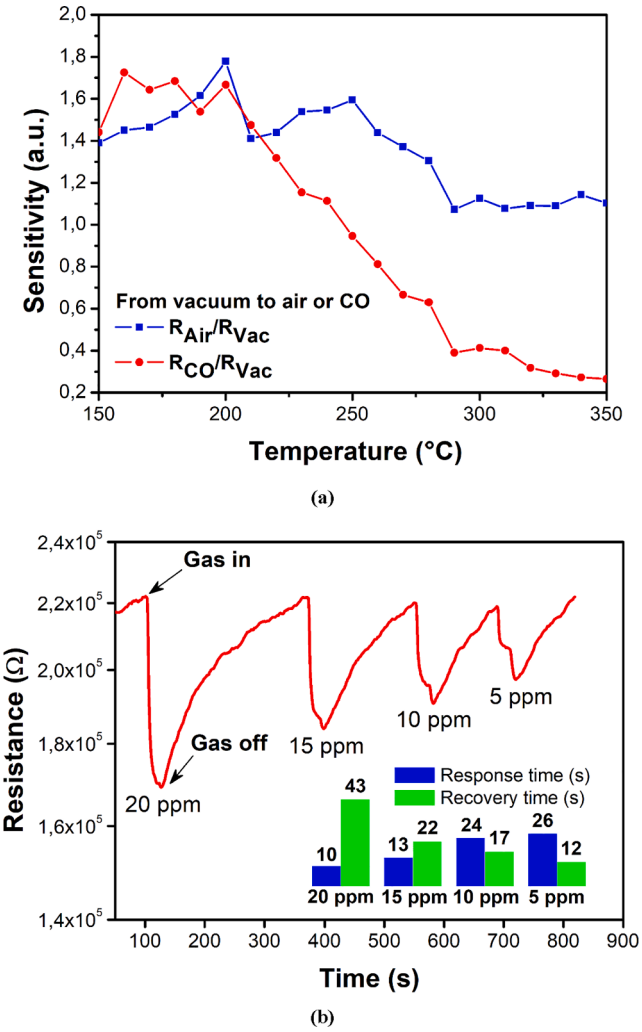

Fig. 10. Sensitivity (a) and sensor response (b) of the films prepared from the ZnO nanorods obtained via the MAH method at 120 °C for 8 min.

20 ppm of CO, the film shows a recovery time (t_{rec}) of 43 s; after 5 ppm of CO, t_{rec} is 12 s. We could see from the FEG-SEM images in Fig. 8 that the film has a porous nature, which enhances its response to CO due to a higher surface area. That is, more oxygen species will adsorb on the surface and react with CO molecules than it would in a non-porous, solid film. The negligible quantity of the surface reaction product and its high volatility indirectly indicates the observed fast response of the nanostructured ZnO sensor to CO and the recovery to initial conditions.

4. Conclusions

We obtained nanostructured zinc oxide via the microwave-assisted hydrothermal (MAH) method at a low temperature and short soaking time. Crystalline ZnO nanorods were formed and no secondary phases were detected. FEG-SEM and TEM analyses have shown a homogeneous size distribution of the nanostructures composed of multiple nanorods. The photoluminescence spectra indicate that the higher emission spectrum of the commercial ZnO sample is associated with a more disordered crystalline structure due to higher bandgap values. The nanostructured ZnO has a lower recombination rate and more charge carriers available to initiate the oxireduction reactions. The photocatalytic performance of the ZnO nanostructures was significantly better than the commercial sample, which we attribute to the superior specific surface area and reduction of the bandgap energy. The ZnO nanostructures reached 50% rhodamine 6-G photodegradation in 17 min while the commercial ZnO

took 43 min to reach the same value. The working temperature of the ZnO nanostructures is around 350 °C, in which the sensitivity to CO was much higher than to air. The sensor film prepared from the ZnO nanostructures showed a fast response time of 10 s to 20 ppm of CO. The photocatalytic and gas sensing performance of the ZnO nanostructures synthesized via the MAH method highlights their multifunctional character and their potential for environmental applications. The use of the MAH method with CTAB is important not only due to short treatment time and low temperatures but also for the possibility to control the morphological, photocatalytic, and sensor properties of the ZnO nanorods.

CRediT authorship contribution statement

P.P. Ortega: Writing - original draft, Writing - review & editing, Formal analysis. **C.C. Silva:** Conceptualization, Methodology. **M.A. Ramirez:** Formal analysis, Writing - review & editing. **G. Biasotto:** Formal analysis, Writing - review & editing. **C.R. Foschini:** Investigation, Writing - review & editing. **A.Z. Simões:** Conceptualization, Methodology, Supervision.

Declaration of Competing Interest

The authors declare that they have no known competing financial interests or personal relationships that could have appeared to influence the work reported in this paper.

Acknowledgments

The financial support of this research project by the Brazilian research funding agency FAPESP is gratefully acknowledged. We would like to thank Frederico Schipani for the sensing measurements and Mario Cilense for FEG-SEM analyses.

References

[1] L. Song, B. Zhang, B. Liu, M. Wu, L. Zhang, L. Wang, S. Xu, Z. Cao, Y. Wang, Effects of maternal exposure to ambient air pollution on newborn telomere length, Environ. Int. 128 (2019) 254–260, https://doi.org/10.1016/j.envint.2019.04.064.
[2] Y. Tang, L. Bi, R. Mortimer, G. Pan, Cryogenic circulation for indoor air pollution control, Sci. Total Environ. 651 (2019) 1451–1456, https://doi.org/10.1016/j.scitotenv.2018.09.220.
[3] C.A. Lin, L.A.A. Pereira, G.M.S. Conceição, H.S. Kishi, R. Milani, A.L.F. Braga, P.H. N. Saldiva, Association between air pollution and ischemic cardiovascular emergency room visits, Environ. Res. 92 (2003) 57–63, https://doi.org/10.1016/S0013-9351(02)00054-3.
[4] A. Tereshchenko, M. Bechelany, R. Viter, V. Khranovskyy, V. Smyntyna, N. Starodub, R. Yakimova, Optical biosensors based on ZnO nanostructures: advantages and perspectives. A review, Sens. Actuators B Chem. 229 (2016) 664-677. https://doi.org/10.1016/j.snb.2016.01.099.
[5] J. Liu, Y. Wang, J. Ma, Y. Peng, A. Wang, A review on bidirectional analogies between the photocatalysis and antibacterial properties of ZnO, J. Alloys Compd. 783 (2019) 898–918, https://doi.org/10.1016/j.jallcom.2018.12.330.
[6] J.E. Contreras, E.A. Rodríguez, Nanostructured insulators – a review of nanotechnology concepts for outdoor ceramic insulators, Ceram. Int. 43 (2017) 8545–8550, https://doi.org/10.1016/j.ceramint.2017.04.105.
[7] S.B. Jagadale, V.L. Patil, S.A. Vanalakar, P.S. Patil, H.P. Deshmukh, Preparation, characterization of 1D ZnO nanorods and their gas sensing properties, Ceram. Int. 44 (2018) 3333–3340, https://doi.org/10.1016/j.ceramint.2017.11.116.
[8] V.S. Bhati, M. Hojamberdiev, M. Kumar, Enhanced sensing performance of ZnO nanostructured-based gas sensor: a review, Energy Rep. (2019), https://doi.org/10.1016/j.egyr.2019.08.070.
[9] S. Suwanboon, P. Amornpitoksuk, P. Bangrak, C. Randorn, Physical and chemical properties of multifunctional ZnO nanostructures prepared by precipitation and hydrothermal methods, Ceram. Int. 40 (2014) 975–983, https://doi.org/10.1016/j.ceramint.2013.06.094.
[10] L. Zhu, Y. Li, W. Zeng, Hydrothermal synthesis of hierarchical flower-like ZnO nanostructure and its enhanced ethanol gas-sensing properties, Appl. Surf. Sci. 427 (2018) 281–287, https://doi.org/10.1016/j.apsusc.2017.08.229.
[11] L.S.R. Rocha, C.R. Foschini, C.C. Silva, E. Longo, A.Z. Simões, Novel ozone gas sensor based on ZnO nanostructures grown by the microwave-assisted hydrothermal route, Ceram. Int. 42 (2016) 4539–4545, https://doi.org/10.1016/j.ceramint.2015.11.145.
[12] R. Ahmad, S.M. Majhi, X. Zhang, T.M. Swager, K.N. Salama, Recent progress and perspectives of gas sensors based on vertically oriented ZnO nanomaterials, Adv. Colloid Interface Sci. 270 (2019) 1–27, https://doi.org/10.1016/j.cis.2019.05.006.
[13] J.H. Kim, A. Mirzaei, H.W. Kim, P. Wu, S.S. Kim, Design of supersensitive and selective ZnO-nanofiber-based sensors for H_2 gas sensing by electron-beam irradiation, Sens. Actuators B Chem. 293 (2019) 210–223, https://doi.org/10.1016/j.snb.2019.04.113.
[14] H. Bai, Z. Liu, D.D. Sun, Hierarchical ZnO nanostructured membrane for multifunctional environmental applications, Colloids Surf. A Physicochem. Eng. Asp. 410 (2012) 11–17, https://doi.org/10.1016/j.colsurfa.2012.05.044.
[15] M.S. Bernardo, P.G. Villanueva, T. Jardiel, D.G. Calatayud, M. Peiteado, A. C. Caballero, Ga-doped ZnO self-assembled nanostructures obtained by microwave-assisted hydrothermal synthesis: effect on morphology and optical properties, J. Alloys Compd. 722 (2017) 920–927, https://doi.org/10.1016/j.jallcom.2017.06.160.
[16] P.P. Ortega, L.S.R. Rocha, J.A. Cortés, M.A. Ramirez, C.A. Buono, M.A. Ponce, A. Z. Simões, Towards carbon monoxide gas sensors based on europium doped cerium dioxide, Appl. Surf. Sci. 464 (2019) 692–699, https://doi.org/10.1016/j.apsusc.2018.09.142.
[17] J. Huang, C. Xia, L. Cao, X. Zeng, Facile microwave hydrothermal synthesis of zinc oxide one-dimensional nanostructure with three-dimensional morphology, Mater. Sci. Eng. B-Adv. 150 (2008) 187, https://doi.org/10.1016/j.mseb.2008.05.014.
[18] W.J. Li, E.W. Shi, W.Z. Zhong, Z.W. Yin, Growth mechanism and growth habit of oxide crystals, J. Cryst. Growth 203 (1999) 186, https://doi.org/10.1016/S0022-0248(99)00076-7.
[19] S. Yamabi, H. Imai, Growth conditions for wurtzite zinc oxide films in aqueous solutions, J. Mater. Chem. 12 (2002) 3773, https://doi.org/10.1039/B205384E.
[20] C. Li, X. Du, W. Lu, K. Liu, J. Chang, S. Chen, D. Yue, Z. Wang, Luminescent single-crystal ZnO nanorods: Controlled synthesis through altering the solvents composition, Mater. Lett. 81 (2012) 229, https://doi.org/10.1016/j.matlet.2012.05.019.
[21] Q. Jiang, Y. Liu, H. Kan, B. Yuan, H. Zhao, Microwave-assisted synthesis of hexagonal structure ZnO micro-tubes, Mater. Lett. 81 (2012) 198, https://doi.org/10.1016/j.matlet.2012.05.012.
[22] M. Baghbanzadeh, S.D. Skapin, Z.C. Orel, C.O. Kappe, A critical assessment of the specific role of microwave irradiation in the synthesis of ZnO micro- and nanostructured materials, Chem.: Eur. J. 18 (2012) 5724, https://doi.org/10.1002/chem.201103548.
[23] H. Cao, Z. Liu, T. Liu, S. Duo, L. Huang, S. Yi, L. Cai, Well-organized assembly of ZnO hollow cages and their derived Ag/ZnO composites with enhanced photocatalytic property, Mater. Charact. 160 (2020) 110125, https://doi.org/10.1016/j.matchar.2020.110125.
[24] P.M. Desimone, C.G. Díaz, J.P. Tomba, C.M. Aldao, M.A. Ponce, Reversible metallization of SnO_2 films under hydrogen and oxygen containing atmospheres, J. Mater. Sci. 51 (2016) 4451–4461, https://doi.org/10.1007/s10853-016-9757-2.
[25] P. Nandi, D. Das, Photocalytic degradation of Rhodamine-B dye by stable ZnO nanostructures with different calcination temperature induced defects, Appl. Surf. Sci. 465 (2019) 546–556, https://doi.org/10.1016/j.apsusc.2018.09.193.
[26] A.P. Moura, R.C. Lima, M.L. Moreira, D.P. Volanti, J.W.M. Espinosa, M.O. Orlandi, P.S. Pizani, J.A. Varela, E. Longo, ZnO architectures synthesized by a microwave-assisted hydrothermal method and their photoluminescence properties, Solid State Ionics 181 (2010) 775–780, https://doi.org/10.1016/j.ssi.2010.03.013.
[27] M.L. Moreira, G.P. Mambrini, D.P. Volanti, E.R. Leite, M.O. Orlandi, P.S. Pizani, V. R. Mastelaro, C.O. Paiva-Santos, E. Longo, J.A. Varela, Hydrothermal Microwave: a new route to obtain photoluminescent crystalline $BaTiO_3$ nano-columns, Chem. Mater. 20 (2008) 5381–5387, https://doi.org/10.1021/cm801638d.
[28] X.M. Sun, X. Chen, Z.X. Deng, Y.D. Li, A CTAB-assisted hydrothermal orientation growth of ZnO nanorods, Mater. Chem. Phys. 78 (2002) 99–104, https://doi.org/10.1016/S0254-0584(02)00310-3.
[29] H. Zhang, D. Yang, Y.J. Ji, X.Y. Ma, J. Xu, D.L. Que, Low temperature synthesis of flowerlike ZnO nanostructures by cetyltrimethylammonium bromide-assisted hydrothermal process, J. Phys. Chem. B 108 (2004) 3955–3958, https://doi.org/10.1021/jp036826f.
[30] S. Komarneni, R. Roy, Q.H. Li, Microwave-hydrothermal synthesis of ceramic powders, Mater. Res. Bull. 27 (1992) 1393–1405, https://doi.org/10.1016/0025-5408(92)90004-J.
[31] U. Coleto, R.A.C. Amoresi, V. Teodoro, I.M. Iani, E. Longo, M.A. Zaghete, L. Perazolli, An approach for photodegradation mechanism at TiO_2/$SrTiO_3$ interface, J. Mater. Sci.: Mater. Elétron. 29 (2019) 20329–20338, https://doi.org/10.1007/s10854-018-0167-x.
[32] M.H. Razali, M.N.A. Fauzi, A.R. Mohamed, S. Sreekantan, Physical properties study of TiO_2 nanoparticle synthesis via hydrothermal method using TiO_2 microparticles as percursor, Adv. Mater. Res. 772 (2013) 365–370, https://doi.org/10.4028/www.scientific.net/AMR.772.365.
[33] R.A.C. Amoresi, V. Teodoro, G.F. Teixeira, M.S. Li, A.Z. Simões, L.A. Perazolli, E. Longo, M.A. Zaghete, Electrosteric colloidal stabilization for obtaining $SrTiO_3$/TiO_2 heterojunction: microstructural evolution in the interface and photonics properties, J. Eur. Ceram. Soc. 38 (2018) 1621–1631, https://doi.org/10.1016/j.jeurceramsoc.2017.10.056.
[34] V.M. Longo, A.T. Figueiredo, S. Lázaro, M.F. Gurgel, M.G.S. Costa, C.O. Paiva-Santos, J.A. Varela, E. Longo, V.R. Mastelaro, F.S. Vicente, A.C. Hernandes, R.W. A. Franco, Structural conditions that leads to photoluminescence emission in $SrTiO_3$: an experimental and theoretical approach, J. Appl. Phys. 104 (2008) 023515, https://doi.org/10.1063/1.2956741.
[35] U. Coleto, R.A.C. Amoresi, C.A.M. Pereira, A.Z. Simões, M.A. Zaghete, E. S. Monteiro, E.S. Filho, E. Longo, L.A. Perazolli, Influence of defects on

photoluminescent and photocatalytic behavior of CaO/$SrTiO_3$ heterojunctions, Ceram. Int. 45 (2019) 15244–15251, https://doi.org/10.1016/j.ceramint.2019.05.013.
[36] Y. Matsumoto, U. Unal, Y. Kimura, S. Ohashi, K. Izawa, Synthesis and photoluminescent properties of titanate layered oxides intercalated with lanthanide cations by electrostatic self-assembly methods, J. Phys. Chem. B. 109 (2005) 12748–12754, https://doi.org/10.1021/jp8038048.
[37] M.Y. Liu, Y.F. Zheng, X.C. Song, One-pot facile synthesis of $AgIO_3$/Ag_2O/Ag nanocomposites with enhanced photocatalytic activity, J. Nanosci. Nanotechnol. 20 (2020) 802–809, https://doi.org/10.1166/jnn.2020.16894.
[38] A. Fujishima, X.T. Zhang, D.A. Tryk, TiO_2 photocatalysis and related surface phenomena, Surf. Sci. Rep. 63 (2008) 515–582, https://doi.org/10.1016/j.surfrep.2008.10.001.
[39] U. Coleto, R.A.C. Amoresi, C.A.M. Pereira, A.Z. Simões, M.A. Zaghete, E.S.M. Filho, E. Longo, L.A. Perazolli, Influence of defects on photoluminescent and photocatalytic behavior of CaO/$SrTiO_3$ heterojunction, Ceram. Int. 45 (2019) 15244–15251, https://doi.org/10.1016/j.ceramint.2019.05.013.
[40] F.T. Bekena, H. Abdullah, D.H. Kuo, M.A. Zeleke, Photocatalytic reduction of 4-nitrophenol using effective hole scavenger over novel Mg-doped Zn(O, S) nanoparticles, J. Ind. Eng. Chem. 78 (2019) 116–124, https://doi.org/10.1016/j.jiec.2019.06.029.
[41] S.V.P. Vattikuti, K.C. Devarayapalli, P.C. Negajyothi, J. Shim, Binder-free WS_2/ZrO_2 hybrid as a photocatalyst for organic pollutant degradation under UV/simulated sunlight and tests for H_2 evolution, J. Alloys Compd. 809 (2019), 151805, https://doi.org/10.1016/j.jallcom.2019.151805.
[42] H. Qin, W. Li, Y. Xia, T. He, Photocatalytic activity of heterostructures based on ZnO and N-doped ZnO, ACS Appl. Mater. Interfaces 3 (2011) 3152–3156, https://doi.org/10.1021/am200655h.
[43] B.H. Toby, EXPGUI, a graphical user interface for GSAS, J. Appl. Crystallogr. 34 (2001) 210–213, https://doi.org/10.1107/S0021889801002242.
[44] W.R.L. Lambrecht, A. Boonchun, Identification of a N-related shallow acceptor and electron paramagnetic resonance center in ZnO:N^{2+} on the Zn site, Phys. Rev. B 87 (2013) 195207, https://doi.org/10.1103/PhysRevB.87.195207.